Crystal Engineering Hot Paper

How to cite: *Angew. Chem. Int. Ed.* **2022,** *61,* e202201234
International Edition: doi.org/10.1002/anie.202201234
German Edition: doi.org/10.1002/ange.202201234

Co-Assembly Induced Solid-State Stacking Transformation in Amino Acid-Based Crystals with Enhanced Physical Properties

Wei Ji[+], Hui Yuan[+], Bin Xue[+], Sarah Guerin, Hui Li, Lei Zhang, Yanqing Liu, Linda J. W. Shimon, Mingsu Si, Yi Cao, Wei Wang, Damien Thompson, Kaiyong Cai, Rusen Yang,* and Ehud Gazit**

Abstract: The physical characteristics of supramolecular assemblies composed of small building blocks are dictated by molecular packing patterns in the solid-state. Yet, the structure–property correlation is still not fully understood. Herein, we report the unexpected cofacial to herringbone stacking transformation of a small aromatic bipyridine through co-assembly with acetylated glutamic acid. The unique solid-state structural transformation results in enhanced physical properties of the supramolecular organizations. The co-assembly methodology was further expanded to obtain diverse molecular packings by different bipyridine and acetylated amino acid derivatives. This study presents a feasible co-assembly approach to achieve the solid-state stacking transformation of supramolecular organization and opens up new opportunities to further explore the relationship between molecular arrangement and properties of supramolecular assemblies by crystal engineering.

Introduction

Hierarchical supramolecular self-assembly with long-range ordered spatial arrangement is a ubiquitous process in nature mediated by multiple non-covalent intermolecular forces.[1] In particular, the organization of simple building blocks into ordered supramolecular structures by a bottom-up approach has gained increasing interest due to the unique properties of the assemblies, along with the advantages of easy preparation and low cost.[2] Typically, the molecular packing motifs, which dictate the physical properties of supramolecular assemblies, can be divided into four types, namely cofacial, brickwork, herringbone, and slipped stacks.[3] For example, while cofacial structure with large surface overlap facilitates efficient charge transport and attenuates the transport anisotropy, the herringbone structure has been revealed as an excellent molecular arrangement for very high charge mobilities in semiconductor materials.[3b,4] Yet, the structure–property correlations between the molecular packing and physical characteristics are still not fully understood as polymorphism is not easy to

[*] Prof. W. Ji,[+] Prof. K. Cai
Key Laboratory of Biorheological Science and Technology, Ministry of Education, The National "111" Project for Biomechanics and Tissue Repair Engineering, College of Bioengineering, Chongqing University
Chongqing 400044 (P. R. China)
E-mail: weiji@cqu.edu.cn

H. Yuan,[+] Prof. E. Gazit
School of Molecular Cell Biology and Biotechnology, George S. Wise Faculty of Life Sciences, Tel Aviv University
Tel Aviv 6997801 (Israel)
E-mail: ehudg@post.tau.ac.il

H. Yuan,[+] Prof. R. Yang
School of Advanced Materials and Nanotechnology, Xidian University
Xi'an 710126 (China)
E-mail: rsyang@xidian.edu.cn

Dr. B. Xue,[+] Prof. Y. Cao, Prof. W. Wang
National Laboratory of Solid State Microstructure, Department of Physics, Nanjing University
Nanjing 210093, Jiangsu (China)

Dr. S. Guerin, Prof. D. Thompson
Department of Physics, Bernal Institute, University of Limerick
Limerick, V94 T9PX (Ireland)

Dr. H. Li
Science and Technology on Combustion and Explosion Laboratory, Xi'an Modern Chemistry Research Institute
Xi'an 710065 (China)

Dr. L. Zhang
CAEP Software Center for High Performance Numerical Simulation
Beijing 100088 (China)

Y. Liu, Prof. M. Si
Key Laboratory for Magnetism and Magnetic Materials of the Ministry of Education, Lanzhou University
Lanzhou 730000 (China)

Dr. L. J. W. Shimon
Department of Chemical Research Support, Weizmann Institute of Science
Rehovot 7610001 (Israel)

[+] These authors contributed equally to this work.

avoid in supramolecular assemblies. Pure, solid-state single crystalline phases are quite challenging to prepare,[5] and this hinders the successful design and control of properties in the desired materials. To overcome this challenge, supramolecular chemists have devoted much effort to chemically modify the molecular structures via small changes that can directly and drastically affect the molecular packing by intermolecular interactions.[6] Different solid-state packing modes were obtained and determined by single crystal structures, precisely establishing the relationships between molecular arrangement and properties of the crystals.[7] However, this approach usually comprises the disadvantages of intricate organic synthesis, static molecular structures, and non-adjustable physical properties, which hinders the development of high-performance organic materials.[8]

Recently, supramolecular co-assembly of multiple component systems inspired by biological materials has emerged as a promising approach to further expand the conformational space of supramolecular assemblies in terms of structural and functional complexity.[1e,9] This methodology paves the way to provide an attractive alternative to time-consuming and inaccessible chemical synthesis and was demonstrated to entail several advantages, such as the control of nanostructure physical dimensions,[10] adjustable mechanical strength,[11] the fabrication of non-canonical complex topologies,[12] switchable fluorescent emissions,[13] and the regulation of the helicity and orientation of nanoarchitectures.[14] In particular, the crystallization of supramolecular co-assembly in the solid state has been demonstrated to be an ideal way to precisely decipher the structure-properties relationships and prepare multifunctional and high performance optoelectronic materials.[15] Although the early stage of co-assembly from small organic molecules was studied recently,[16] the basic interaction mechanism and principles underlying the co-crystallization process are still unclear. Furthermore, not every potential pair of donor and acceptor can co-assemble and crystallize as the criteria for co-crystal formation are quite restrictive.[5b] The effective tuning of the physical properties of the co-crystals by designing and controlling the transformation of molecular stacking modes remains a challenge.[17]

Herein, we report an unexpected transformation from cofacial to herringbone stacking of a small aromatic bipyridine (BPY) by co-assembly with a non-aromatic acetylated glutamic acid (AcE) (Figure 1). The co-assembly between BPY and AcE was thoroughly characterised by fluorescence microscopy, powder X-ray diffraction (PXRD), circular dichroism (CD), Raman spectroscopy, and nuclear magnetic resonance (NMR). The solid-state stacking modes of supramolecular assemblies were determined by single-crystal X-ray diffraction. In the single crystal state, BPY could form intermolecular hydrogen bonding with water molecules resulting in cofacial molecular arrangements. However, by adding AcE as the conformer, BPY preferably formed intermolecular hydrogen bonding with AcE rather than with solvent molecules, leading to herringbone molecular arrangements. The unique stacking transformation resulted in modulation of the physical properties of the co-crystal, including morphology, fluorescence emission, supramolecular chirality, thermal stability, mechanical property, band structure and piezoelectricity. Furthermore, diverse molecular packing modes were obtained through the co-assembly between different bipyridine and acetylated amino acid derivatives. This study directly demonstrates the co-assembly induced supramolecular stacking transformation in the solid state by crystal engineering and promotes

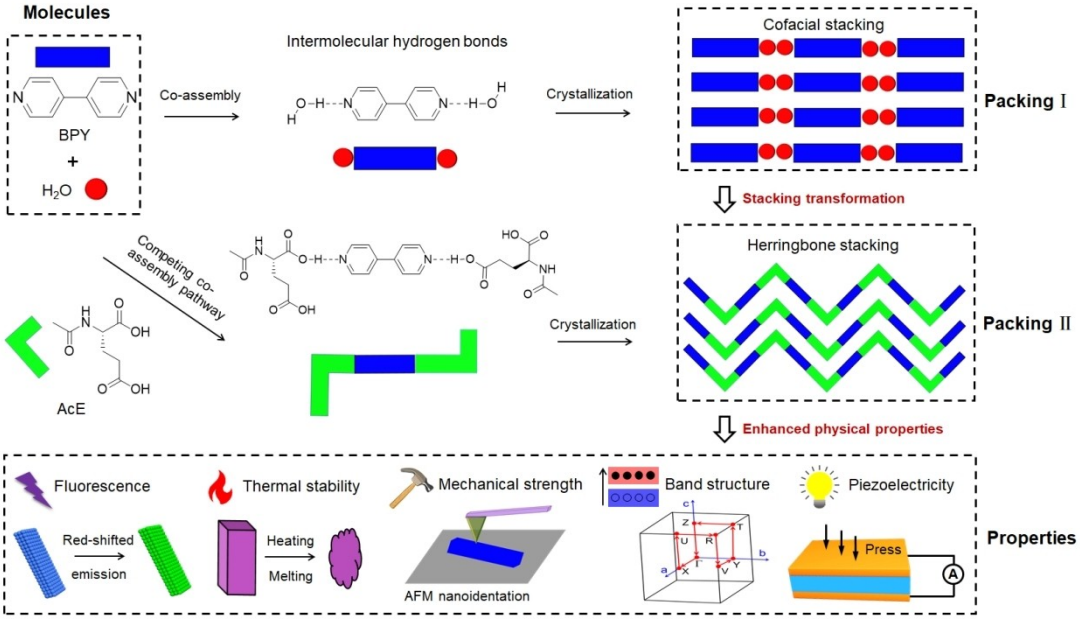

Figure 1. Schematic presentation of co-assembly induced stacking transformation from cofacial to herringbone packing in molecular crystals, leading to enhanced physical properties of the crystals.

the precise understanding of the relationship between molecular packing and properties of supramolecular assemblies.

Results and Discussion

Based on the affinity of intermolecular hydrogen bonding between the carboxylic acid group and the pyridine ring,[18] a molar ratio of BPY/AcE (1:1) was chosen for the co-assemblies, denoting the equal number of two pyridine and two carboxylic acid groups in the chemical structures of BPY and AcE, respectively. BPY self-assembled to form long needle-shaped crystals, which could emit blue fluorescence under UV light excitation due to the aromatic nature of BPY (Figure 2a). Needle-shaped crystals were also observed in the self-assembly of AcE, that could not emit fluorescence (Figure 2b). However, bulk irregular needles were observed for the BPY/AcE mixture (Figure 2c), and red-shifted emission from blue to green was found for the BPY/AcE mixture, suggesting the different packing mode of BPY in the new crystalline state. Compared to the pure BPY and AcE crystals, the appearance of new peaks (11.24°, 28.36°, 30.30°) and the absence of several original peaks (10.47°, 12.41°, 12.74°, 13.72°, 21.62°, 23.61°) was observed in the PXRD of BPY/AcE, indicating a new molecular arrangement (Figure 2d). Furthermore, the supramolecular chirality of the crystal samples was evaluated by CD (Figure 2e). A positive Cotton effect was observed at 226 nm for pure AcE crystals while pure BPY crystals did not produce a CD signal. In contrast, a much higher intensity of ellipticity and different Cotton effects (two positive peaks at 208 and 252 nm, two negative peaks at 288 and 342 nm) were detected in the co-assembly state, reflecting the enhanced

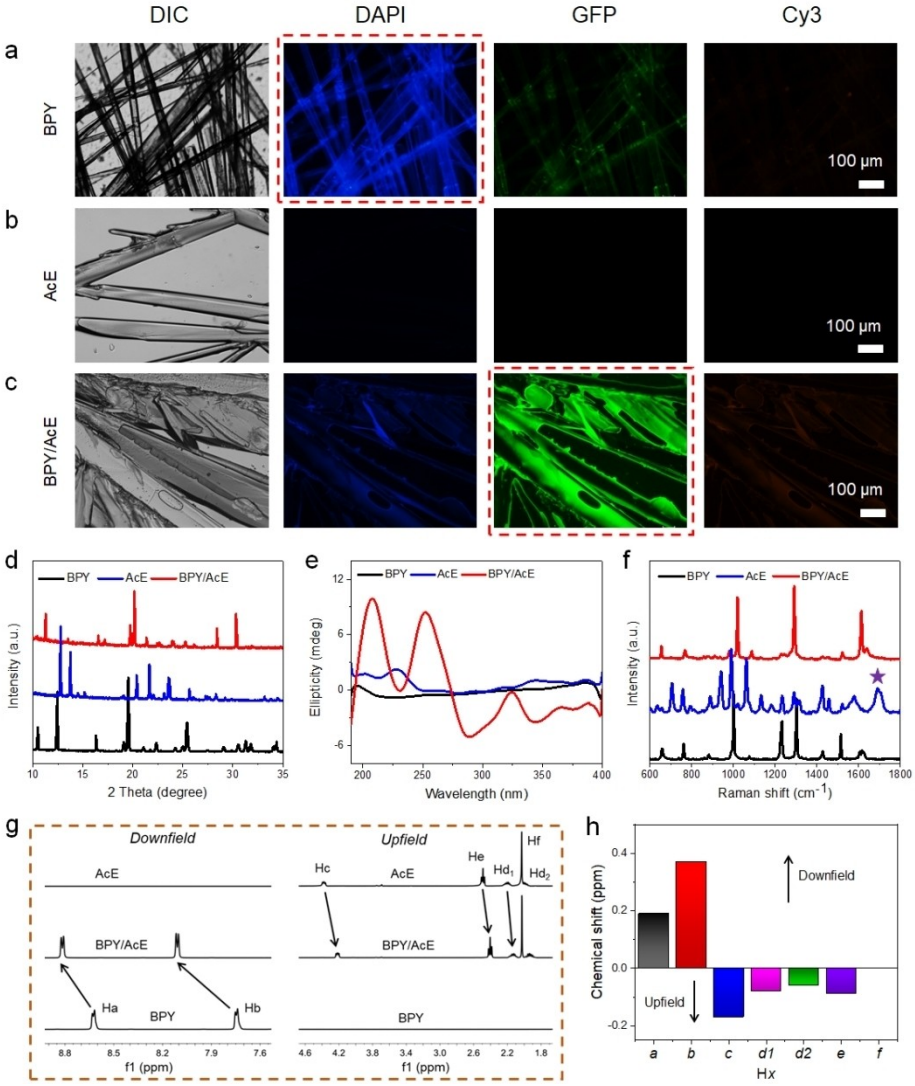

Figure 2. a)–c) Microscopy images of a) BPY, b) AcE, and c) BPY/AcE crystals in bright field (DIC, differential interference contrast, on the left) and in different fluorescence channels, as indicated. d) PXRD analysis of the BPY, AcE, and BPY/AcE crystals. e) CD spectra of the BPY, AcE, and BPY/AcE crystals. f) Raman spectra of the BPY, AcE, and BPY/AcE crystals. g) ^{1}H NMR spectra of BPY, AcE, and BPY/AcE. h) Chemical shift of ^{1}H NMR of BPY/AcE, compared to the single component BPY and AcE.

supramolecular chirality of the co-crystals with high asymmetric supramolecular organizations.

Raman spectrum and ^{1}H NMR spectra were examined to elucidate the intermolecular hydrogen bonding between the carboxylic acid group of AcE and the pyridine ring of BPY during co-assembly. The peak at 1693 cm^{-1} ascribed to the C=O stretching vibration of the carboxylic acid in AcE was absent due to the formation of hydrogen bonding between carboxylic acid and pyridine in the BPY/AcE co-assembly (Figure 2f). The labels of hydrogen atoms in the chemical structures of BPY (*Ha*, *Hb*) and AcE (*Hc, Hd, He, Hf*) are shown in Figure S1 for the analysis of ^{1}H NMR experiments. An obvious downfield shift was observed for the hydrogen atoms of BPY after co-assembly with AcE. In contrast, an upfield shift was found for the hydrogen atoms of AcE (Figure 2g,h). These results confirmed the formation of a BPY/AcE complex with strong intermolecular hydrogen bonding between carboxylic acid and pyridine.

To better understand the molecular packing modes in the pure crystals and co-crystal at the atomic level, diffraction quality crystals were grown from methanol and their structures were thoroughly analysed by single crystal X-ray diffraction.[19] Detailed crystal data collection and refinement parameters of the BPY crystal and BPY/AcE co-crystal are summarized in Table S1. BPY crystallized in the monoclinic space group $P2_1$ with two BPY molecules and four water molecules in the asymmetric unit (Figure 3a, b, Figure S3). Intermolecular hydrogen bonding was found between the N atom in BPY and H atom in water molecules (Figure S4a). First, each N atom interacted with one water molecule (N1···H2A–O2) through hydrogen bond with a N···H distance of 2.096 Å, which further connected the next BPY molecule via another water molecule (O2–H2B···O1) with a O···H distance of 1.894 Å. The other connected intermolecular N2···H1B–O1 hydrogen bond length was 2.128 Å, forming a 1D molecular chain. Second, the water-mediated single molecular chains of BPY further formed 3D crystal networks by cofacial π–π stacking interactions between pyridine rings with distances of 3.705 and 3.712 Å and hydrogen bonds between water molecules with O···H distance of 1.929 Å (Figure S4b). Thus, pure BPY molecules could form classic cofacial crystal stacking through the formation of intermolecular hydrogen bonding with solvent molecules (Figure 3c). AcE crystallized in the orthorhombic space group $P2_12_12_1$ with one AcE molecule in the asymmetric unit (Figure 3d and S2).[20] The AcE molecule was directly hydrogen bonded to four adjacent molecules by a total of six hydrogen bonds (Figure 3e and Figure S5). Two cyclic dimer hydrogen bonds were formed by two N–H6···O25 and O15–H5···O21 contacts with bond lengths of 1.799 (O25···H6) Å and 2.105 Å (O21···H5), respectively. Furthermore, an additional tight hydrogen bond O11-H1···O5 with a shorter distance of 1.528 Å (O5···H1) facilitated the 3D crystal network formation. A layer-by-layer arrangement was observed in the higher order crystal packing of AcE (Figure 3f).

Compared to the individual crystal structures, co-crystallization of BPY and AcE resulted in the formation of a new crystal containing one molecule of BPY and one molecule of AcE in the asymmetric unit with a completely distinct molecular arrangement, which crystallized in the monoclinic space group $P2_1$ (Figure 3g, Figure S6). As indicated by Raman and ^{1}H NMR experiments, the hydrogen bonds between the carboxylic acid group of AcE and the pyridine ring of BPY were directly observed in the crystal structures (Figure 3h). BPY formed a strong trimer with two molecules of AcE stabilized through two intermolecular hydrogen bonds (O2–H2···N2 and O4–H4···N3, Figure S7a) with distances of 1.814 Å (N2···H2) and 1.817 Å (N3···H4), respectively. Compared to the hydrogen bond between BPY and water molecules in the single crystal (N···H distance: 2.096 Å and 2.128 Å), the shorter hydrogen bonds between BPY and AcE indicates strong pairing in the co-crystal. The trimer of BPY with two AcE molecules showed an angle of ≈58° directed by the two intermolecular hydrogen bonds, which propagated to form a classic herringbone stacking mode in the higher order packing of the co-crystal structure (Figure 3i). No face-to-face π–π stacking between aromatic rings was found due to the long centre-to-centre distance (5.747 Å) (Figure S7b). Thus, the direct observation of solid-state cofacial to herringbone stacking transformation was validated in the crystal structure of BPY through co-assembly with AcE. We further performed density functional theory (DFT) calculations to visualise the valence charge density distribution and Hirshfeld surface of the crystals using the HASEM code. The result and analysis were shown in Figure S8.

The thermal stability of the single- and co-crystals was evaluated by thermogravimetric analysis (TGA) and differential scanning calorimetry (DSC) analyses (Figure S9a–c). The TGA results revealed that the BPY and AcE single crystals remained stable until the temperature reached 107.5°C and 191.5 °C, respectively. After co-crystallization, the BPY/AcE crystal degraded only after the temperature reached 155.6 °C. Endothermic peaks were observed in the DSC curve: BPY (70.3 °C, 112.1 °C, 188.0 °C), AcE (192.8 °C, 235.5 °C), and BPY/AcE (171.7 °C, 223.1 °C). The morphological changes and thermal events of the crystals were further investigated using hot-stage optical microscopy (HSOM) to visually examine thermal transitions (Figure S9d–f). Melting of the three crystals was observed at a decomposition temperature range of approximately 111.2–112 °C, 193–200.4 °C, and 162–172 °C for BPY, AcE, and BPY/AcE, respectively. Thus, the thermal stability order is [AcE > BPY/AcE > BPY], suggesting that co-assembly with the more thermally-stable conformer of AcE, producing a new herringbone packing, could improve the thermal stability relative to pure BPY with a cofacial packing.

Investigating the mechanical properties of molecular crystals has long been a subject of considerable interest to chemists due to their versatile applications in pharmaceutical technology, biophysics, polymer science, and optoelectronic devices.[21] To examine the effect of molecular packing modes on the mechanical properties of the crystals, atomic force microscopy (AFM)-based nanoindentation experiments were performed by applying the AFM cantilever tip to the surface of the crystalline needles. Typically, the surface of the crystals was scanned using the AFM tapping

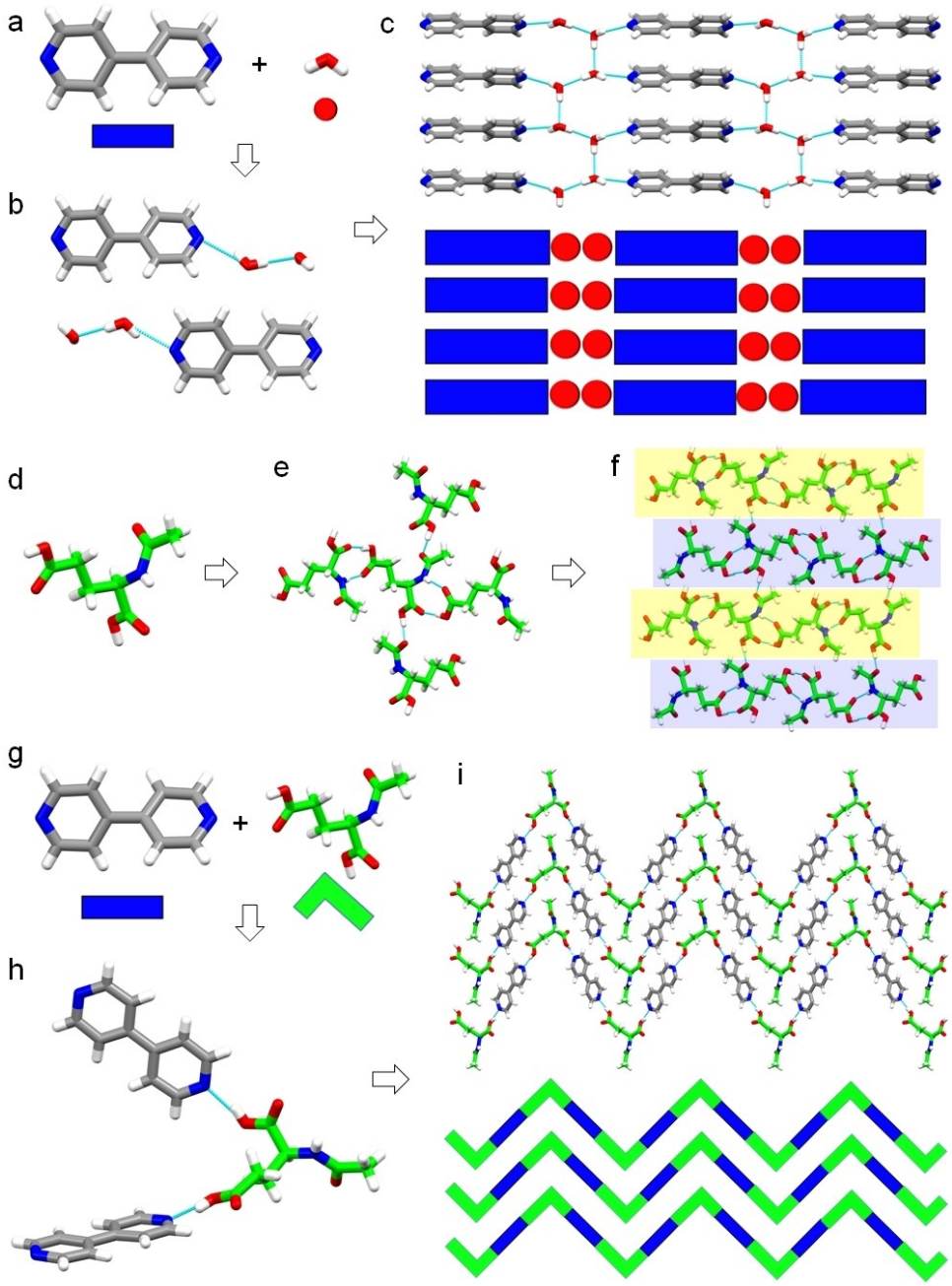

Figure 3. a) Chemical structures of BPY and water molecules in the crystals. b) Intermolecular hydrogen bonding formation between BPY and water molecules. c) Higher order of cofacial crystal stacking between BPY and water molecules. d) The AcE molecule asymmetric building unit. e) The formation of hydrogen bonds between adjacent AcE molecules. f) Supramolecular layer-by-layer arrangement in the higher order crystal packing of AcE. The two molecular packing layers are denoted in yellow and blue. g) BPY and AcE molecules combine via h) intermolecular hydrogen bonding between the BPY pyridine ring and AcE carboxylic acid groups. i) Higher order of herringbone crystal stacking between BPY and AcE molecules.

mode to locate the smaller size flat area (Figure S10). Then the cantilever was forced to press the flat area and retracted at a constant speed of 30 $\mu m\,s^{-1}$ (Figure 4a), during which the force-displacement traces were recorded. The Young's modulus of the crystals at different positions could be determined by fitting the retracting traces using the Hertz model (Figure 4b and Figure S11). Both Young's modulus and point-stiffness were evaluated to study the mechanical rigidity. The topographic Young's modulus maps showed the Young's moduli for the pure crystals of BPY (Figure 4c), AcE (Figure 4d), and the BPY/AcE co-crystal (Figure 4e). The histogram distribution of Young's modulus was further analysed, showing the statistical values of Young's modulus along the thickness direction to be 15.3 ± 4.9 GPa (Figure 4f), 16.6 ± 2.6 GPa (Figure 4g), and 83.4 ± 10.7 GPa (Figure 4h) for BPY, AcE, and BPY/AcE, respectively. Moreover, the value of point stiffness could also be calculated according to the force-displacement traces (Figure S12). The

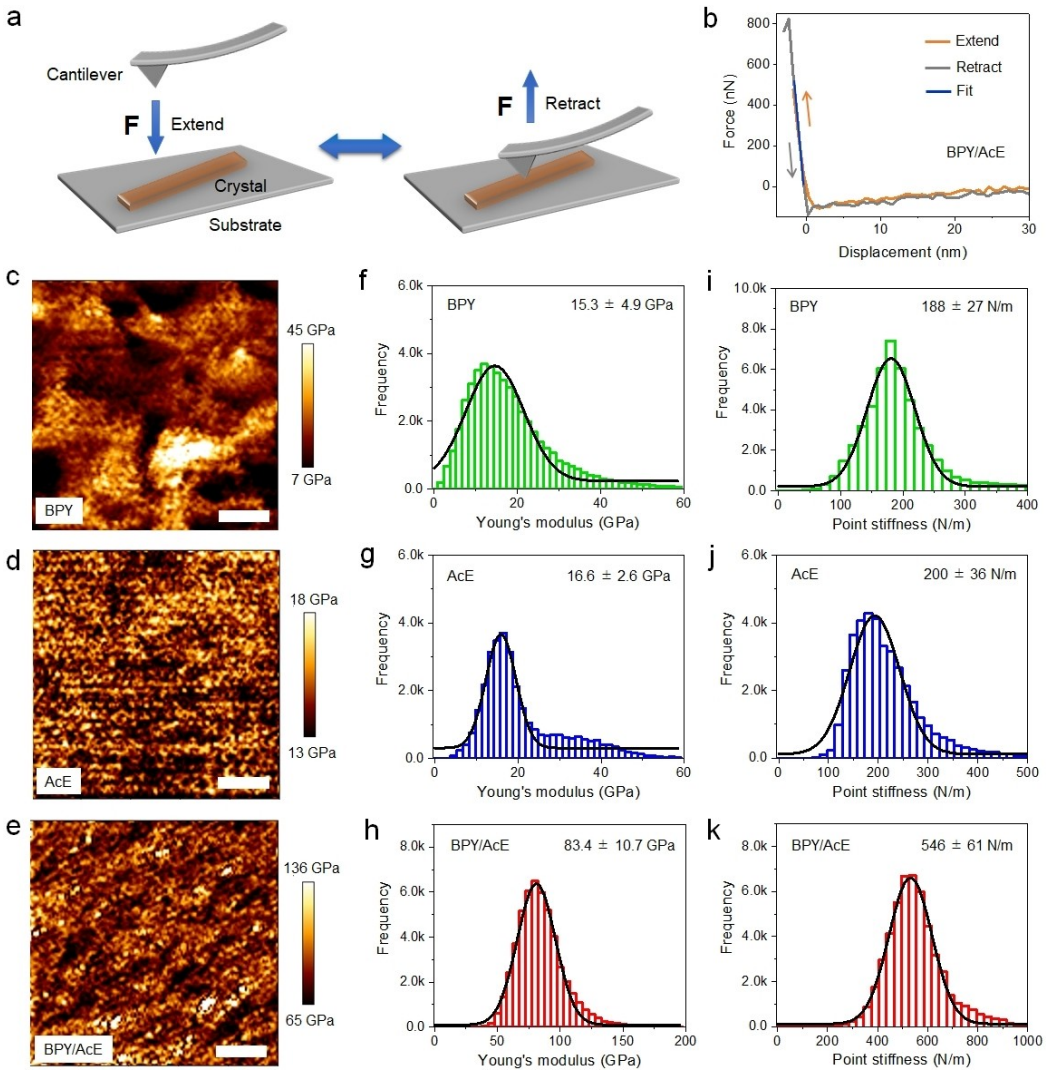

Figure 4. a) Schematic diagram of AFM indentation experiments performed on crystal samples. b) Typical force-displacement traces on the BPY/AcE co-crystal. c)–e) Topographic modulus maps of c) BPY, d) AcE, and e) BPY/AcE. Scale bar is 100 nm. f)–h) The statistical Young's modulus distributions of f) BPY, g) AcE, and h) BPY/AcE. i)–k) The statistical point stiffness distributions of i) BPY, j) AcE, and k) BPY/AcE.

statistical point stiffness values of single- and co-crystals were $188 \pm 27\ N\,m^{-1}$ (Figure 4i), $200 \pm 36\ N\,m^{-1}$ (Figure 4j), and $546 \pm 61\ N\,m^{-1}$ (Figure 4k) for BPY, AcE, and BPY/AcE, respectively. Thus, the rigidity order is [BPY/AcE > AcE > BPY], indicating an enhanced mechanical stiffness by co-crystallization due to the tightly-packed supramolecular organization of herringbone stacking through the combination of intermolecular interactions.

We further explored the electric band structures and density of states (DOS) properties of the three crystals by first-principle calculations. The corresponding 3D packing structures in different directions are shown in Figure S13. The first Brillouin zones of the primitive cells of the three crystals are displayed in Figure S14. The calculated electronic band structures and the corresponding DOS of the three crystals as shown in Figure 5a and Figure S15 demonstrate the indirect band gap of the BPY/AcE co-crystal to be approximately 2.96 eV, in the semiconductor range. In contrast, both single crystals of BPY and AcE showed larger indirect band gap values of approximately 4.79 eV and 4.94 eV, respectively. The plotted orbital charge density of conduction band minimum (CBM) and valence band maximum (VBM) surfaces (Figures S16–S18) show that the VBM and CBM of BPY/AcE were both not located at high symmetry points. The charge densities of CBM were only located in the structures of the BPY molecules, while in the VBM, the charge densities were distributed in the structure of the AcE molecules (Figure 5b). The intermolecular binding of BPY with AcE decreased its band gap relative to the individual components, suggesting potential future application for the BPY/AcE co-crystal as an indirect band gap semiconductor.

The non-centrosymmetric structure of the three crystals suggests piezoelectric responses owing to the supramolecular internal polarization. We predicted the piezoelectric properties of the crystals by DFT calculations. The optimised

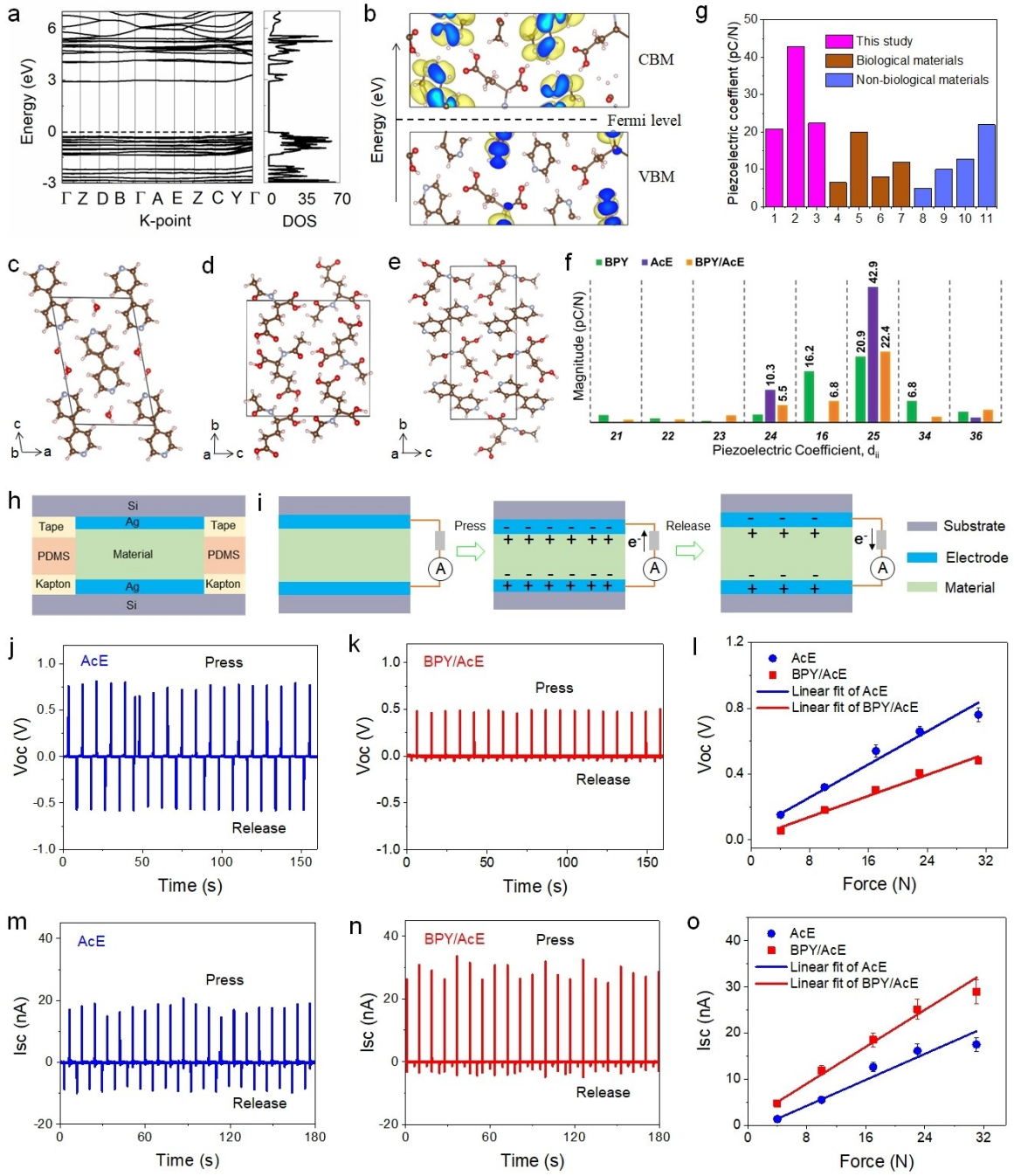

Figure 5. a) Band structures and density of states of the BPY/AcE co-crystal. b) Computed orbital charge densities of CBM and VBM bands of the BPY/AcE co-crystal along the *a* axis. c)–e) Optimized crystal structures of c) monoclinic BPY, d) orthorhombic AcE, and e) monoclinic BPY/AcE. f) Predicted absolute piezoelectric strain constants, d_{ij} of all three crystals. g) Comparison of the maximum piezoelectric coefficients of selected different biological (brown) and non-biological (blue) materials, as well as BPY, AcE, and BPY/AcE crystals (pink). 1: BPY, 2: AcE, 3: BPY/AcE, 4: lysozyme, 5: gelatin nanofiber, 6: chitosan, 7: asparagine, 8: aluminium nitrate, 9: poly (lactic acid), 10: GaN nanowires, 11: PVDF. The relevant references are shown in Table S6. h) Schematic presentation of the preparation and sandwich structure of the piezoelectric nanogenerators. i) Piezoelectric energy conversion process of the sandwich-structured generator by press and release using molecular crystals as active components. j), k) Open-circuit voltage of j) AcE and k) BPY/AcE crystal-based generators obtained by applying a force of 31 N. l) Linear fitting of the open-circuit voltage of AcE and BPY/AcE crystal-based nanogenerator. m), n) Short-circuit current of m) AcE and n) BPY/AcE crystal-based generator obtained by applying a force of 31 N. o) Linear fitting of the short-circuit current of AcE and BPY/AcE crystal-based nanogenerator.

structures of the three crystals used for prediction are shown in Figure 5c–e. The orthorhombic symmetry of the AcE crystal allows for three shear piezoelectric tensor components only, compared to eight for the monoclinic BPY and BPY/AcE crystals (Tables S3–S5). A slight increase in the piezoelectric charge constant e_{23} was observed in the co-

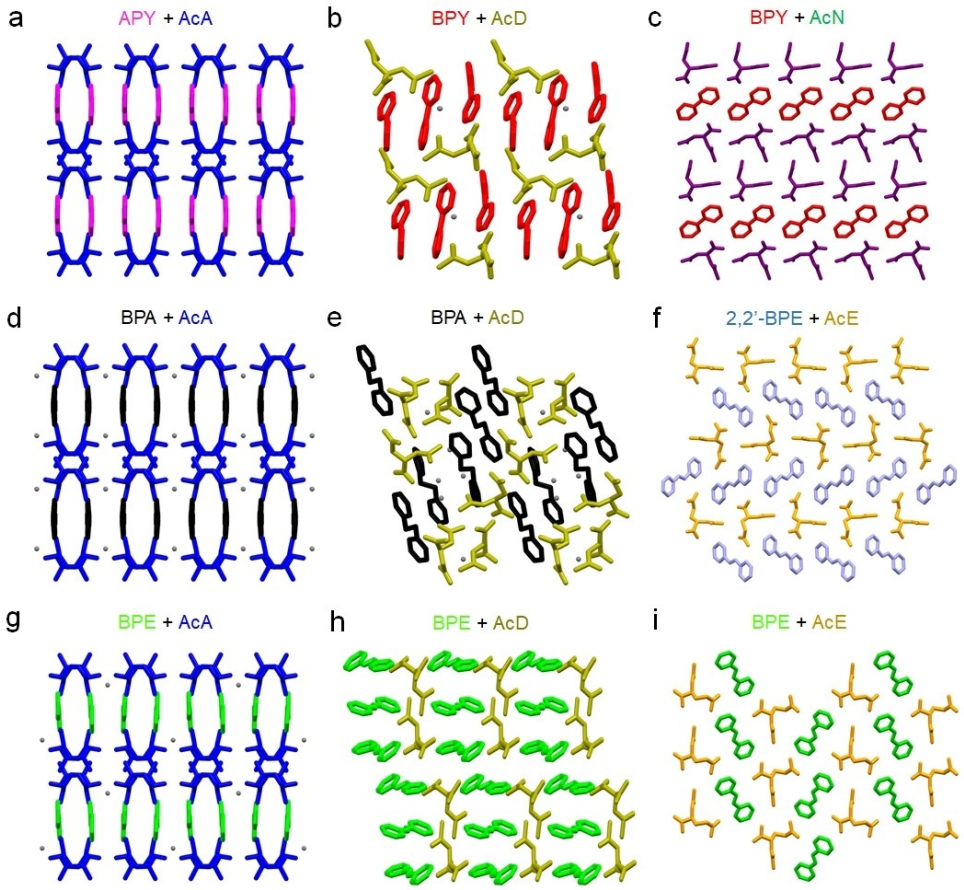

Figure 6. Higher order of different crystal stacking between bipyridine and acetylated amino acid molecules viewed along their *a* axes: a) APY/AcA, b) BPY/AcD, c) BPY/AcN, d) BPA/AcA, e) BPA/AcD, f) 2,2′-BPE/AcE, g) BPE/AcA, h) BPE/AcD, and i) BPE/AcE. The different colours indicate different molecules to more clearly depict the different molecular packing.

crystals with a value of 0.03 Cm^{-2}. The maximum piezoelectric strain constants (d_{max}) did not increase with co-crystallisation, showing values in-between those of BPY and AcE crystals (Figure 5f). The highly flexible AcE single crystal showed the highest piezoelectric response, with a large predicted d_{25} value of 42.9 pCN^{-1}. The AcE crystal has favourable packing of its carboxyl groups that facilitates strong intermolecular interactions in all directions, and thus large ionic displacement under an applied shear force. The maximum response of the co-crystal is significant, with d_{25} of 22.4 pCN^{-1}, and is slightly higher than the highest maximum response in BPY single crystals. The d_{max} values of the three crystals were comparable to different biological and non-biological materials (Figure 5g and Table S6), including biological materials such as lysozyme (6.5 pCN^{-1}), gelatin nanofiber (20 pCN^{-1}), chitosan (8 pCN^{-1}), and asparagine (12 pCN^{-1}), and non-biological materials such as aluminium nitrate (5 pCN^{-1}), poly (lactic acid) (10 pCN^{-1}), GaN nanowires (12.8 pCN^{-1}), and PVDF (22 pCN^{-1}). The relevant references are shown in Table S6. Furthermore, all three crystals showed significant piezoelectric voltage constants, indicating their potential for energy harvesting applications. The calculated g_{max} values were 1151, 1670, and 784 mV m/N for BPY, AcE and BPY/AcE, respectively, higher than that of lead zirconium titanate (PZT) and many of its lead-free counterparts ($g_{max} = 250$ $mV\,m\,N^{-1}$), the piezoelectric materials most widely exploited for sensing and actuation.[22] A summary of the knowledge on the structural and chemical features that modulate piezoelectric performance in molecular co-crystals was shown in Supporting Information (Page S20).

We further studied the piezoelectric properties of the three crystals powders by designing and fabricating sandwich power generators. The schematic of a fabricated crystal material-based nanogenerator and the energy conversion process are depicted in Figure 5h and i. The applied force-dependent open-circuit voltages and short-circuit currents of crystal film-based nanogenerators were both tested in the pressing force range from 0 N to 31 N. By applying a pressing force of 31 N, the values of open-circuit voltage reached up to 0.42 V, 0.73 V, and 0.47 V for BPY, AcE and BPY/AcE, respectively, confirming the DFT-predictions of significant voltage output from the co-crystal and highest piezoelectric response of AcE single crystals (Figure 5j–k and Figures S19–S21). Particularly, the applied force-dependent open-circuit voltages from 4 N to 31 N showed a good linear fit (Figures 5l, S19f, S20f, and S21f), indicating the stable piezoelectric response of the three crystals for the

voltage signals. These values exceed the value achieved by other piezoelectric nanogenerators based on inorganic materials (e.g. ZnO, monolayer MoS_2) and biological materials (e.g. M13 bacteriophage).[23] Moreover, the open-circuit voltage produced by the power nanogenerator maintained at a constant level at different pressing and releasing points, suggesting useful dielectric property and negligible current leakage during the energy conversion process. By applying a pressing force of 31 N, the values of short-circuit currents were found to be 0.57 nA, 17.40 nA, and 27.86 nA for BPY, AcE and BPY/AcE, respectively (Figure 5m,n and Figures S22–S24). Furthermore, a good linear fit was also observed for the applied force-dependent short-circuit currents (Figure 5o, Figures S22f, S23f, and S24f), indicating the piezoelectric response of these molecular crystals for the current output. The BPY/AcE co-crystal generated the highest short-circuit current output due to its lower resistance, which is in good agreement with the calculated band structures and DOS profiles of the crystals. These results revealed the potential application of the fabricated nanogenerators based on organic molecular crystals in energy harvesting with tunable piezoelectricity.

The criteria for co-crystal formation are quite restrictive since not every pair of donor and acceptor can co-assemble and crystallize, thus, we further changed the chemical structures of BPY and AcE into different bipyridine and acetylated amino acid derivatives and investigated whether more co-crystal structures can be obtained by using this co-assembly methodology (Figure S25). From these experiments, nine diffraction-quality co-crystals were grown from methanol and their structures were thoroughly analyzed, including APY/AcA, BPY/AcD, BPY/AcN, BPA/AcA, BPA/AcD, 2,2′-BPE/AcE, BPE/AcA,[24] BPE/AcD, and BPE/AcE, demonstrating the generality of this co-assembly methodology. Detailed crystal data collection and refinement parameters of these co-crystals are summarized in Supporting Information Tables S7 and S8. The hydrogen bonds and higher order of crystal stacking between bipyridine and acetylated amino acid molecules were analysed and are shown in Figure S26 and Figure 6. Intermolecular hydrogen bonds between the pyridine ring of bipyridines and the carboxylic acid group of acetylated amino acids was observed in all the crystal structures as the driving force for co-assembly. Different crystal packing modes were generated by the co-crystallization of the two types of molecules denoted by different colours (Figure 6). From this detailed investigation of the molecular platform, we found that bipyridine derivatives like BPY, BPA, BPE, showed a good tendency to form co-crystals with acetylated amino acids (AcA, AcD, AcE). Interestingly, strong AcA dimers stabilized through two face-to-face intermolecular hydrogen bonds were observed in all AcA-based co-crystals (APY/AcA, BPA/AcA, BPE/AcA), which acted as the bridge to cage the bipyridine molecules and further produced similar supramolecular packing modes (Figure S26a, S26d, S26 g and Figure 6a,d,g). Compared to other acetylated amino acids, the molecular structures of AcD and AcE have two carboxylic acid groups with different geometry, increasing the possibility of molecular co-assembly between the pyridine ring and the carboxylic acid to form higher-order supramolecular organizations (Figure S26b, S26e, S26f, S26h, S26i and Figure 6b,e,f,h,i).

Conclusion

In summary, we present the co-assembly induced solid-state cofacial to herringbone stacking transformation, as validated by X-ray crystallography, using very simple molecular building blocks. The effect of supramolecular packing on the physical properties of the resulting crystals is thoroughly investigated by various experimental methods and DFT calculations. Compared to BPY hydrate crystals with cofacial stacking, co-crystallization with AcE molecules to form a new herringbone stacking resulted in modified physicochemical properties of the crystals, such as red-shifted fluorescence emission, enhanced supramolecular chirality, improved thermal stability, increased mechanical strength and reduced band gap. Moreover, high values of force-dependent open-circuit voltage and short-circuit current were generated by fabricating sandwich piezoelectric devices using AcE and BPY/AcE crystals, respectively, making them promising candidates for energy harvesting. Moreover, the co-assembly methodology was expanded to obtain diverse molecular packings using different bipyridine and acetylated amino acid derivatives. This study not only demonstrates a feasible co-assembly strategy to regulate the solid-state packing transformation of minimal molecular building blocks into supramolecular organizations with enhanced physical properties, but also provides new insights to precisely establish the structure–property correlations in multiple-component crystals and further inspire the rational molecular design of high-performance organic optoelectronic materials for next-generation sustainable and energy-efficient technologies.

Experimental Section

Experimental procedures and supplementary data were described in the Supporting Information.

Acknowledgements

This work was supported by the Fundamental Research Funds for the Central Universities (No. 2021CDJQY-021 and 020414380187), the European Research Council under the European Union Horizon 2020 research and innovation program (No. 694426), the National Natural Science Foundation of China (No. 52103148, 51973170 and 11804148), the Natural Science Foundation of Jiangsu province (No. BK20180320). Science Foundation Ireland (SFI) under awards number 15/CDA/3491 and 12/RC/2275 P2. W. J. acknowledges the support of the Start-up Funding from Chongqing University. The authors thank Dr. Sigal Rencus-Lazar for language editing assistance.

Conflict of Interest

The authors declare no conflict of interest.

Data Availability Statement

The data that support the findings of this study are available from the corresponding author upon reasonable request.

Keywords: Amino Acids · Co-Assembly · Stacking Modes · Supramolecular Chemistry

[1] a) M. P. Hendricks, K. Sato, L. C. Palmer, S. I. Stupp, *Acc. Chem. Res.* **2017**, *50*, 2440–2448; b) M. J. Webber, E. A. Appel, E. W. Meijer, R. Langer, *Nat. Mater.* **2016**, *15*, 13–26; c) J. Li, J. Wang, H. Li, N. Song, D. Wang, B. Z. Tang, *Chem. Soc. Rev.* **2020**, *49*, 1144–1172; d) K. Tao, P. Makam, R. Aizen, E. Gazit, *Science* **2017**, *358*, eaam9756; e) D. M. Raymond, B. L. Nilsson, *Chem. Soc. Rev.* **2018**, *47*, 3659–3720; f) A. Lampel, S. A. McPhee, H. A. Park, G. G. Scott, S. Humagain, D. R. Hekstra, B. Yoo, P. W. J. M. Frederix, T. D. Li, R. R. Abzalimov, S. G. Greenbaum, T. Tuttle, C. Hu, C. J. Bettinger, R. V. Ulijn, *Science* **2017**, *356*, 1064–1068; g) T. P. J. Knowles, R. Mezzenga, *Adv. Mater.* **2016**, *28*, 6546–6561; h) I. W. Hamley, *Chem. Rev.* **2017**, *117*, 14015–14041; i) K. Ariga, X. F. Jia, J. W. Song, J. P. Hill, D. T. Leong, Y. Jia, J. B. Li, *Angew. Chem. Int. Ed.* **2020**, *59*, 15424–15446; *Angew. Chem.* **2020**, *132*, 15550–15574.

[2] a) X. H. Yan, P. L. Zhu, J. B. Li, *Chem. Soc. Rev.* **2010**, *39*, 1877–1890; b) L. Adler-Abramovich, E. Gazit, *Chem. Soc. Rev.* **2014**, *43*, 6881–6893; c) H. M. Wang, Z. Q. Q. Feng, B. Xu, *Chem. Soc. Rev.* **2017**, *46*, 2421–2436; d) P. Xing, Y. Zhao, *Adv. Mater.* **2016**, *28*, 7304–7339.

[3] a) Z. F. Yao, J. Y. Wang, J. Pei, *Cryst. Growth Des.* **2018**, *18*, 7–15; b) K. Zhou, H. Dong, H. Zhang, W. Hu, *Phys. Chem. Chem. Phys.* **2014**, *16*, 22448–22457.

[4] P. Gómez, S. Georgakopoulos, J. P. Cerón, I. Da Silva, M. Más-Montoya, J. Pérez, A. Tárraga, D. Curiel, *J. Mater. Chem. C* **2018**, *6*, 3968–3975.

[5] a) T. He, M. Stolte, C. Burschka, N. H. Hansen, T. Musiol, D. Kälblein, J. Pflaum, X. Tao, J. Brill, F. Würthner, *Nat. Commun.* **2015**, 65954; b) P. Yu, Y. Zhen, H. Dong, W. Hu, *Chem* **2019**, *5*, 2814–2853.

[6] a) S. J. Yoon, S. Varghese, S. K. Park, R. Wannemacher, J. Gierschner, S. Y. Park, *Adv. Opt. Mater.* **2013**, *1*, 232–237; b) W. J. Geng, Q. Ma, Y. Chen, W. Yang, Y. F. Jia, J. S. Li, Z. Q. Zhang, G. J. Fan, S. M. Wang, *Cryst. Growth Des.* **2020**, *20*, 2106–2114; c) J. Dhar, D. P. Karothu, S. Patil, *Chem. Commun.* **2015**, *51*, 97–100.

[7] a) W. Jiang, Y. Li, Z. H. Wang, *Chem. Soc. Rev.* **2013**, *42*, 6113–6127; b) X. Zhang, H. Dong, W. Hu, *Adv. Mater.* **2018**, *30*, 1801048; c) C. Yuan, W. Ji, R. R. Xing, J. B. Li, E. Gazit, X. H. Yan, *Nat. Chem. Rev.* **2019**, *3*, 567–588.

[8] Q. Wang, Q. Zhang, Q. W. Zhang, X. Li, C. X. Zhao, T. Y. Xu, D. H. Qu, H. Tian, *Nat. Commun.* **2020**, *11*, 158–166.

[9] a) P. Makam, E. Gazit, *Chem. Soc. Rev.* **2018**, *47*, 3406–3420; b) E. R. Draper, D. J. Adams, *Chem. Soc. Rev.* **2018**, *47*, 3395–3405.

[10] L. Adler-Abramovich, P. Marco, Z. A. Arnon, R. C. G. Creasey, T. C. T. Michaels, A. Levin, D. J. Scurr, C. J. Roberts, T. P. J. Knowles, S. J. B. Tendler, E. Gazit, *ACS Nano* **2016**, *10*, 7436–7442.

[11] a) B. O. Okesola, Y. Wu, B. Derkus, S. Gani, D. Wu, D. Knani, D. K. Smith, D. J. Adams, A. Mata, *Chem. Mater.* **2019**, *31*, 7883–7897; b) S. Bera, S. Mondal, Y. Tang, G. Jacoby, E. Arad, T. Guterman, R. Jelinek, R. Beck, G. Wei, E. Gazit, *ACS Nano* **2019**, *132*, 1703–1712.

[12] S. Yuran, Y. Razvag, M. Reches, *ACS Nano* **2012**, *6*, 9559–9566.

[13] G. A. Hudalla, T. Sun, J. Z. Gasiorowski, H. Han, Y. F. Tian, A. S. Chong, J. H. Collier, *Nat. Mater.* **2014**, *13*, 829–836.

[14] a) J. Y. Liu, F. Yuan, X. Ma, D. Y. Auphedeous, C. C. Zhao, C. Liu, C. Shen, C. L. Feng, *Angew. Chem. Int. Ed.* **2018**, *57*, 6475–6479; *Angew. Chem.* **2018**, *130*, 6585–6589; b) F. Wang, C. L. Feng, *Angew. Chem. Int. Ed.* **2018**, *57*, 5655–5659; *Angew. Chem.* **2018**, *130*, 5757–5761; c) X. Q. Dou, N. Mehwish, C. C. Zhao, J. Y. Liu, C. Xing, C. L. Feng, *Acc. Chem. Res.* **2020**, *53*, 852–862.

[15] a) P. Xing, Y. Zhao, *Acc. Chem. Res.* **2018**, *51*, 2324–2334; b) L. Sun, Y. Wang, F. Yang, X. Zhang, W. Hu, *Adv. Mater.* **2019**, *31*, 1902328; c) L. Sun, F. Yang, X. Zhang, W. Hu, *Mater. Chem. Front.* **2020**, *4*, 715–728.

[16] a) C. Yuan, A. Levin, W. Chen, R. Xing, Q. Zou, T. Herling, P. Challa, T. Knowles, X. Yan, *Angew. Chem. Int. Ed.* **2019**, *58*, 18116–18123; *Angew. Chem.* **2019**, *131*, 18284–18291; b) C. Yuan, M. Yang, X. Ren, Q. Zou, X. Yan, *Angew. Chem. Int. Ed.* **2020**, *59*, 17456–17460; *Angew. Chem.* **2020**, *132*, 17609–17613.

[17] a) M. Karimi-Jafari, L. Padrela, G. M. Walker, D. M. Croker, *Cryst. Growth Des.* **2018**, *18*, 6370–6387; b) H. T. Black, D. F. Perepichka, *Angew. Chem. Int. Ed.* **2014**, *53*, 2138–2142; *Angew. Chem.* **2014**, *126*, 2170–2174; c) Y. Huang, Z. Wang, Z. Chen, Q. Zhang, *Angew. Chem. Int. Ed.* **2019**, *58*, 9696–9711; *Angew. Chem.* **2019**, *131*, 9798–9813.

[18] A. Lemmerer, D. A. Adsmond, C. Esterhuysen, J. Bernstein, *Cryst. Growth Des.* **2013**, *13*, 3935–3952.

[19] Deposition Numbers 2102646 (for BPY), 2102647 (for BPY/AcE), 2127021 (for APY/AcA), 2126954 (for BPY/AcD), 2126952 (for BPY/AcN), 2127020 (for BPA/AcA), 2127019 (for BPA/AcD), 2127022 (for 2,2′-BPE/AcE), 2127128 (for BPE/AcD), and 2127018 (for BPE/AcE) contain the supplementary crystallographic data for this paper. These data are provided free of charge by the joint Cambridge Crystallographic Data Centre and Fachinformationszentrum Karlsruhe Access Structures service.

[20] A. J. Dobson, R. E. Gerkin, *Acta Crystallogr. Sect. C* **1997**, *53*, 73–76.

[21] a) S. Varughese, M. S. R. N. Kiran, U. Ramamurty, G. R. Desiraju, *Angew. Chem. Int. Ed.* **2013**, *52*, 2701–2712; *Angew. Chem.* **2013**, *125*, 2765–2777; b) G. R. Krishna, R. Devarapalli, G. Lal, C. M. Reddy, *J. Am. Chem. Soc.* **2016**, *138*, 13561–13567; c) S. Saha, M. K. Mishra, C. M. Reddy, G. R. Desiraju, *Acc. Chem. Res.* **2018**, *51*, 2957–2967.

[22] T. R. Shrout, S. J. Zhang, *J. Electroceram.* **2007**, *19*, 113–126.

[23] a) Y. Qiu, H. Zhang, L. Hu, D. Yang, L. Wang, B. Wang, J. Ji, G. Liu, X. Liu, J. Lin, F. Li, S. Han, *Nanoscale* **2012**, *4*, 6568–6573; b) S. K. Kim, R. Bhatia, T. H. Kim, D. Seol, J. H. Kim, H. Kim, W. Seung, Y. Kim, Y. H. Lee, S. W. Kim, *Nano Energy* **2016**, *22*, 483–489; c) B. Y. Lee, J. X. Zhang, C. Zueger, S. W. J. Chung, Y. Yoo, E. Wang, J. Meyer, R. Ramesh, S. W. Lee, *Nat. Nanotechnol.* **2012**, *7*, 351–356.

[24] W. Ji, B. Xue, S. Bera, S. Guerin, L. J. W. Shimon, Q. Ma, S. A. M. Tofail, D. Thompson, Y. Cao, W. Wang, E. Gazit, *Mater. Today* **2021**, *42*, 29–40.

Manuscript received: January 24, 2022
Accepted manuscript online: February 15, 2022
Version of record online: March 2, 2022